Cryo-EM structures of the translocational binary toxin complex CDTa-bound CDTb-pore from *Clostridioides difficile*

Akihiro Kawamoto
Osaka University https://orcid.org/0000-0002-7380-0127
Tomohito Yamada
Kyoto Sangyo University
Toru Yoshida
Japan Women's University
Takayuki Kato
Osaka University https://orcid.org/0000-0002-8879-6685
Hideaki Tsuge (tsuge@cc.kyoto-su.ac.jp)
Kyoto Sangyo University https://orcid.org/0000-0003-0166-9163

Article

Keywords: C. difficile toxin, actin ADP-ribosylation, translocation pore

Posted Date: November 1st, 2021

DOI: https://doi.org/10.21203/rs.3.rs-1018941/v1

Version of Record: A version of this preprint was published at Nature Communications on October 17th, 2022. See the published version at https://doi.org/10.1038/s41467-022-33888-4.

Abstract

Besides two large cytotoxins (TcdA and TcdB), certain *Clostridioides difficile* strains also produce a binary toxin, called *C. difficile* toxin (CDT) composed of an enzymatic subunit involved in actin ADP-ribosylation (CDTa) and translocation pore (CDTb) that delivers CDTa into host cells through receptor-mediated endocytosis. CDTb is proposed to be a di-heptamer, but its physiological heptameric structure has not been reported to date. Here, we report the CDTa-bound CDTb-pore (heptamer) as a physiological complexes using cryo-EM. The high-resolution structure of the CDTa-bound CDTb-pore at 2.56-Å resolution revealed that CDTa binding to CDTb-pore induces partial unfolding and tilting of the first CDTa a-helix, and the translocation. In the CDTb-pore, the NSS-loop exists in “in” and “out” conformations, suggesting their involvement in substrate translocation through formation of weak, non-specific interactions. This structural information provides insights into drug design against hypervirulent *C. difficile* strains.

Introduction

Transport of proteins across lipid membranes is an essential biological process[1]. Many protein transport systems, including translocation pores, translocation channels, or translocons, have been reported in eukaryotes and prokaryotes. In co-translational transport, the translocon associates with the ribosome so that a nascent polypeptide chain is threaded through the channel as an unfolded protein chain[2,3]. On the other hand, some proteins need to be transported after being folded. For example, to be translocated across the narrow pore, the effectors of the type III secretion system need to be unfolded into a secretion competent state by unfoldases or chaperones [4–6]. Additionally, some bacteria have a unique translocation system named binary toxin, which is comprised by a substrate A-component that translocates across the membrane via a B-component of the toxin. The B-component was shown to be involved in the binding of the toxin to host cells, thereby allowing protein unfolding and the translocation of the enzymatic A-component into the cytosol[7–10]. Among such binary toxins are *Clostridium perfringens* iota toxin (Ia and Ib), *Clostridium spiroforme* toxin (CSTa and CSTb), *Clostridium botulinum* C2 toxin (C2I and C2II), and *Clostridioides difficile* (previously known as *Clostridium difficile*) toxin (CDTa and CDTb)[11]. These binary toxins exhibit sequence similarity in both A- and B-components (Supplementary Fig. S1). The B-component binds to the target cell through a common receptor—the lipolysis-stimulated lipoprotein receptor (LSR)—in *C. perfringens* iota toxin, *C. difficile* toxin, and *C. spiroforme* toxin[12,13], after which the toxin A–B complex is internalized by receptor-mediated endocytosis. Then, the A-component is transported via the B-component pore across the endoplasmic membrane into the cytosol[14], a translocation step that is assisted by the host cell chaperones, such as Hsp90 or Hsp70[15,16]. In the cytosol, the A-component covalently transfers an ADP-ribose to actin, causing F-actin depolymerization, cell rounding, and eventually cell death[17,18]. Structural and functional studies on the A-component of the clostridial binary toxin have shown that the enzymatic component consists of two domains: the C-terminal domain with ADP-ribosyltransferase activity and the N-terminal domain that functions as the B-component binding domain[19–22]. The *Bacillus anthracis* anthrax toxin belongs to

another group of binary toxins that comprise an enzymatic component (two enzymatic proteins, edema [EF] and lethal [LF] factors) and a protein translocation channel (protective antigen [PA])[23]. In binary toxins among the first and second groups, there are major differences in the activity and structure of their enzymatic A-components; however, it has been considered that their B-components have functional and structural similarities.

C. difficile infection causes hospital-acquired diarrhoea and mortality. In the United States, nearly half a million people are diagnosed with *C. difficile* infection and approximately 15,000 deaths are directly attributed to *C. difficile* infection in a single year (CDC digital press, Feb 2015). In addition to the two large clostridial glycosylating cytotoxins (TcdA and TcdB), certain strains of *C. difficile* produce the binary toxin CDT[24–26]. For example, the hypervirulent *C. difficile* 027/BI/NAP1 produces CDT in addition to TcdA and TcdB[27,28]. Another hypervirulent strain, 078/BK/NAP, also produces CDT[29–31]. Whether CDT promotes virulence is debatable; however, CDT can depolymerise actin, leading to the formation of microtubule base protrusions, thereby increasing pathogen adherence[32]. Furthermore, CDT induces host inflammation through the toll-like receptor 2-dependent pathway, resulting in the suppression of the protective host eosinophilic response[33]. Thus, a synergistic effect of different toxins could lead to hypervirulence.

Several structures of the CDTb oligomer have been reported. Anderson et al. reported an asymmetric dimer of heptamers, called the short form, which consists of a pore state stacked with a non-inserted pre-pore state at 3.7-Å resolution (PDB ID: 6O2N, C7 symmetry), and a symmetric dimer of heptamers, called the long form, which consists of two partial β-barrel states at 3.9-Å resolution (PDB ID: 6O2M, C7 symmetry)[34]. Xu et al. also reported the same short form structure at 2.8-Å resolution (PDB ID: 6UWR) using cryo-EM and at 3.7-Å resolution (PDB ID: 6UWI)[35] using X-ray crystallography. In addition, they reported another symmetric dimer of heptamers consisting of two pre-pore states at 3.1-Å resolution (PDB ID: 6UWT). In these heptameric dimer structures, the receptor binding D4 domain (D4II) forms a heptameric static ring, which interacts with another heptameric static ring through hydrophobic loop–loop interactions (Leu772 and Phe774). These di-heptameric states are inadequate for CDT pore formation in the membrane and CDTa translocation across the membrane. In contrast, heptameric state of CDTb have also been reported with CDTa (N-terminal (1–16 deficient mutant) in the presence of the LSR (PDB ID: 6V1S), which prevents heptamer dimerization through the D4II domains[36]. These structures called pre-insertion states, are different from pre-pore and pore states, and represent a conformation in transition from pre-pore to pore. However, in this structure, the LSR and D4II domains show no visible density because of their fluctuation, and information on the binding between CDTa and CDTb is lacking as the resolution is limited to 3.8-Å. Importantly, the physiological state of the heptameric CDTb-pore and the process by which CDTb interacts with and transports CDTa across the cell membrane remain unclear.

Here, we report two cryo-EM structures of the CDTa-bound CDTb-pore: classes 1 and 2 at 2.64- and 2.56-Å resolution, respectively. Both structures show that one CDTa molecule binds to the heptameric CDTb subunit through its N-terminal domain. Overall, our findings reveal the interaction between CDTa and CDTb based on the high-resolution structure of the CDTa-bound CDTb-pore (class 2). Binding induces the

unfolding and tilting of the first N-terminal α-helix of CDTa, in addition to conformational changes to one of the constriction sites in the CDTb-pore, called the NSS-loop, which grips CDTa. Assessment of the dynamic features of the NSS-loop revealed that they exist in two conformations, namely "in" and "out" states, which interconversion seem to be essential for translocation process in binary toxins comprising CDT and iota toxin.

Results

Preparation of the CDTb heptameric pore

To prepare the heptameric CDTb-pore, we used a solubilization protocol similar to that used for preparing the iota toxin pore with lauryl maltose neopentyl glycol (LMNG), which mimics the buried liposome environment[31,37]. This protocol differed from the CDTb-pore preparation protocol[34]. For Ib-pore sample preparation, the Ib oligomer was purified using density-gradient ultracentrifugation after pro-peptide cleavage by trypsin, which induced oligomerization in 10% ethanol, at a low concentration of LMNG. In the case of CDTb, cleavage of the pro-peptide by trypsin induced oligomerization without ethanol, but it caused the dimerization of the heptamers, as previously reported[34,35]. We considered that the dimer of heptamers was an artefact under solution conditions without a membrane lipid because it was formed by covering the hydrophobic region of the pore from a hydrophilic solvent. Thus, CDTb-pores were prepared by pro-peptide cleavage followed by oligomerization in LMNG-containing buffer at 37°C. LMNG served to cover the CDTb hydrophobic regions, allowing its solubilization. Furthermore, to obtain CDTa-bound CDTb-pores, CDTa was added to the purified CDTb-pore at a 3-fold molar excess.

Unexpectedly, three-dimensional (3D) classification revealed three classes: one included a di-heptamer and the other two classes included heptamer pores of CDTa-bound CDTb-pores (classes 1 and 2) (Supplementary Fig. S2). The ratios of the di-heptamer, class 1 pore, and class 2 pore were of approximately 1.2:1.0:2.0 (particle numbers 102,116; 83,061; and 173,260; respectively). The map of the di-heptamer at 3.19-Å revealed that it consisted of a pore state stacked with a non-inserted pre-pore state, as revealed by the previous study of CDTb (PDB ID: 6UWR). However, CDTa molecules were observed in each heptamer at the top and bottom sites. Unfortunately, CDTa density was averaged out in the map even at C1 map calculation (Fig. 1, Supplementary Fig. S2). By contrast, CDTa-bound CDTb-pores (classes 1 and 2) showed clear CDTa density in their maps (Fig. 1, Supplementary Fig. S2). The final resolutions of the CDTa-bound CDTb-pores (classes 1 and 2) were of 2.64 and 2.56-Å, respectively, based on the "gold-standard" Fourier shell correlation (FSC) 0.143 cut-off criterion[38,39]. Because reports on CDTa-bound CDTb-pores are lacking, we focused on two structures, namely CDTa-bound CDTb-pores (classes 1 and 2) (Table 1). In particular, the detailed interactions between CDTa and CDTb were analysed using the CDTa-bound CDTb-pore (class 2), which was subjected to the focused 3D classification around CDTa, with excellent map quality (Supplementary Fig. S3).

Overall structures of classes 1 and 2 of CDTa-bound CDTb-pores

We solved two structures of CDTa-bound CDTb-pores (Fig. 2a-2d). Class 1 CDTa-bound CDTb-pore seemed to contain one whole β-barrel stem; however, the final map calculation showed that the tip of the β-barrel stem (residues 337–358) had very weak density; therefore, we modelled the structure with a partial β-barrel stem (residues 337–358 were excluded). By contrast, class 2 CDTa-bound CDTb-pore did not contain one whole β-barrel stem. Thus, both class 1 and 2 CDTa-bound CDTb-pores have a partial β-barrel stem lacking residues 337–358 and 332–363 from the tip of the β-barrel, respectively. A definitive difference between the two structures included D4II, which was observed in the class 1 but not in the class 2 CDTa-bound CDTb-pore complex. However, the two overall structures were similar, including the 1:1 binding ratio of CDTa:CDTb-pore. CDTa contained two domains: the N-terminal domain that binds CDTb and that C-terminal domain has ADP-ribosyltransferase activity (Fig. 2a), and CDTb comprised four domains: 1' (W214–A296: domain 1 without the pro-peptide), 2 (Y297–I513), 3 (S514–P616), and 4 (T617–D876) (Fig. 2b). The main pore body comprised domain 2, which consisted of two parts designated 2c (297–312 and 382–513 aa) and 2s (313–381 aa). Domain 2s was an extended β-hairpin, with seven copies assembled to form a membrane-spanning 14-stranded β-barrel. Domain 3 was located at an intermediate position between domains 1' and 2c, and domain 4 (D4I). Domain 4 is the receptor-binding domain that was located at the outermost region of the pore, comprising two sub-domains, D4I (T617–L741) and D4II (T757–D876), which were joined through a linker (N742–P756), as seen in class 1.

The lumen of the pore contained four constriction sites: three and one were located on the *cis* and *trans* sides of the pore, respectively (Fig. 2e and 2f). The first constriction site comprised a unique N-terminal di-calcium binding site, designated Ca-edge, with a 45-Å inner diameter. The second constriction site comprised the NSS-loop (491–493 aa), with a 23-Å inner diameter. The importance of the Ca-edge and NSS-loop in CDTa-binding is described later. The narrowest clamp was formed by seven Phe residues (F455) from seven protomers with an inner diameter of 6-Å, which was called ϕ-clamp and was first described in the PA pore[40]. The ϕ-clamp is a stable region in the structure. The fourth constriction site was composed of H314, located in the stem just below the ϕ-clamp. H314 had a density of two conformers and was conserved in the family.

CDTa-binding mode and translocational unfolding of CDTa in the CDTb-pore

In both class 1 and 2 complexes, CDTa was bound to the *cis*-side of the CDTb-pore through its N-terminal domain (Fig. 2c and d). One-half of the CDTa N-terminal domain was buried in the CDTb-pore through several interactions with Ca-edges and NSS-loops. The interface area was estimated at 1,960-Å^2. Five Ca-edges from subunits C, D, E, F and G contributed the interaction with the CDTa N-terminal domain (Fig. 2g, Supplementary Table 1). Notably, four (C–F) NSS-loops were found to play an important role in gripping CDTa. These interactions caused conformational changes in the NSS-loops. 2.56-Å resolution analysis provided more precise insights into the NSS-loops, with "in" and "out" conformations being clearly observed (Fig. 3). In the A, B, and G subunits, which shows almost no interaction with the CDTa via NSS-loop, the NSS-loop clearly showed two conformations. Furthermore, in the D and E subunits, the NSS-loop showed two conformations. However, in the C and F subunits, the NSS-loop only existed in the "out"

conformation because of the interaction with CDTa. We did not determine the pore structure without CDTa in this manuscript; therefore, we checked the di-heptamer structure at 2.8-Å resolution (PDB ID: 6UWR), which is a di-heptamer complex of pore and pre-pore states. Interestingly, we found that both "in" and "out" states could be seen in the pore and pre-pore states in the cryo-EM map as described later. However, conformations deposited in PDB (ID: 6UWR) are in the "in" for the pore and "out" for the pre-pore states, respectively. Thus, we conclude that the NSS-loop conformation is in equilibrium between the two states in the default pore structure. Then, the interactions with CDTa biased their NSS-loop conformations to fit or catch CDTa, especially in the C and F subunits.

The two α-helices (a1–a2) at the N-terminus of CDTa penetrated deeply into the pores (Fig. 2e and 2g). The binding with CDTb induced partial unfolding of the first N-terminal α-helix of CDTa. The N-terminus included 19-WERKEAER-26 in the presented complex and 10-LKDKEKAKEWERKEAER-26 in the crystal structure (PDB ID: 2WN6); therefore, the nine residues at the N-terminus in the first α-helix were unfolded (Fig. 4). The unfolding of the α-helix could be caused by steric hindrance between CDTa and CDTb. Moreover, the first N-terminal α-helix of CDTa in the complex showed tilting with an inclination of approximately 20° compared with the crystal structure of CDTa, which suggests that the tip of the N-terminal α-helix was heading to the φ-clamp (Fig. 4).

Discussion

We obtained three different classes of CDTa-bound CDTb-pore from sample preparation with LMNG. Though di-heptamer structure also coexisted with single-heptamers, the CDTa map was averaged out even at C1 map calculation. Therefore, we determined two high-resolution structures of heptameric CDTa-bound CDTb-pores, shedding light into CDTa-CDTb interactions. The structures of classes 1 and 2, with other reported structures of CDTb, including di-heptamers, are summarised in Supplementary Fig. S4. *Cis* and *trans* interactions of the D4II receptor-binding domains have been reported to form di-heptamers of CDTb[34,35], with F774 being the key amino acid in the *trans* interaction. This amino acid is mutated to Leu in Ib, and thus, in vitro, Ib mostly forms a heptamer and not a di-heptamer[41]. At low concentrations, CDTb would exist as a single heptamer to exert its pathogenic effects. Conversely, at high concentrations, CDTb di-heptamer will be stable and may be protected from aggregation or proteolysis.

The overall structures of Ia-bound Ib-pores and CDTa-bound CDTb-pores were similar. Both used their conserved constriction site Ca-edge and NSS-loop (Ib:NSQ-loop) for A-component binding. Ca-edges are di-calcium binding sites that consist of DTDNDNIPDSYE in CDTb and DTDNDNIPDAYE in Ib. Di-calcium densities were clearly observed in both Ib and CDTb[41]. The ϕ-clamp is formed by seven Phe residues (F455 in CDTb and F454 in Ib) from seven protomers and has an inner diameter of 6-Å[41]. The conformations of Phe residues in CDTb and Ib were similar, in which these side-chain densities are clearly visible. Although the NSS-loop, substituted by the NSQ-loop in Ib, is not perfectly conserved, it functions to grip the A-component in both CDTb and Ib, making it an essential structural element. Although NSS-loop is important for CDTa binding, the strong binding between CDTa and CDTb seems to inhibit the efficient translocation of CDTa. To overcome this constrain, the binding between CDTa and CDTb need to

be loosen and not specific during the translocation. In this study, we found two conformations of NSS-loop designated "in" and "out" (Fig. 5, Supplementary Fig. S5), indicating that two stable states—instead of many flexible states—exist in the NSS-loop. The two conformations were also observed in the map density in the pre-pore and pore structures of CDTb (Supplementary Fig. S5). Although we assigned "in" conformations to NSQ-loops in the Ib pore structure[41], we re-examined the Ia-bound Ib-pore map and structure (PDB ID: 6KLO), which allowed to observe a weaker density of the "out" conformation than that of "in" (Fig. 5). These results show that two conformations of NSS-loop (NSQ-loop in Ib) are common in the binary toxin family, including in CDT and iota toxin. Given that the binding between CDTa and CDTb need to be not so strong, flipping between the "in" and "out" states seems to enable the efficient translocation of the substrate. In other words, a transient intermediate would associate through weak non-specific interactions via the flipping of the NSS-loops.

The structure of the anthrax toxin PA-pore has been determined in its apo form[18], and EF- and LF-bound forms[42] by cryo-EM. The atomic structures of the LF-and EF-bound forms show that the first helix unfolds and docks into a deep amphipathic cleft, called the α-clamp, which is located between the two Ca-edges of PA. The binding modes of EF and LF are similar, as both use the first α-helix to bind the α-clamp, and the 20–30 N-terminal residues are missing, possibly continuing to the φ-clamp located 35–40-Å away. The structure of the PA-pore shows a striking similarity to the CDTb-pore and Ib-pore. However, the substrate components differ in their activity, structure, and binding mode between CDTa/Ia and LF/EF. Structurally, CDTb and Ib have the α-clamp in similar regions, where two adjacent Ca-edges are created, but both CDTb and Ib do not use the region for α-helix binding. In the PA-pore, the α-clamp was proposed to be important for the non-specific binding of the α-helix and subsequent translocation. The α- and φ-clamps appear to operate allosterically, with peptide binding at the α-clamp site being required for the allosteric gating of the φ-clamp to a clamped state[43]. In the CDTb-pore and Ib-pore, an α-clamp is not needed for binding; instead, these pores use a different way to unfold the N-terminal α-helix. In the CDTa-bound CDTb-pore, CDTb binding induces disorder of the nine N-terminal residues in the first α-helix (10-LKDKEKAKE-18). The same region is unfolded in the Ia-bound Ib-pore, with Ib inducing the disorder of the loop region in the crystal structure (3-IERPEDFLK-11) and further unfolding of the α-helix in the crystal structure (12-DKENAI-17). In both CDTa-bound CDTb-pore and Ia-bound Ib-pore, the N-terminus of the A-component starts at almost the same position in the complex (18 in Ia and 19 in CDTa) (Fig. 4). Notably, a similar tilting of the first N-terminal α-helix in CDTa and Ia, which is heading toward the φ-clamp, was observed in their pore complexes (Fig. 4). In summary, both pore complex structures allowed limited space for the first α-helix due to steric hindrance between the substrate protein and the pore. The distance between the N-terminus of the first α-helix and the φ-clamp was of 25–30-Å. We propose that the unstructured N-terminal regions of CDTb and Ib are essential for translocation via the φ-clamp, through a mechanism that can be explained using the extended-chain Brownian ratchet model[44]. The first step of threading through the narrow φ-clamp is the most challenging, similar to threading a needle, with the subsequent translocation proceeding smoothly via the DpH-driven Brownian ratchet model. For this purpose, the CDTb- and Ib-pore systems use a common mechanism to unfold the N-terminus region of the substrate, which is induced by steric hindrance. Notably, the extended N-terminus regions of CDTa

and Ia are protected in a similar hydrophilic environment, except for the φ-clamp inside the *cis*-side of the pore (Supplementary Fig. S6). Furthermore, both CDTb- and Ib-pore systems use a common dynamic mechanism: the dynamic structure of the NSS(NSQ)-loop, which offers advantages for the translocation of intermediate proteins with neither strong nor weak interactions (Fig. 6). These unique features of the binding and the unfolding are observed in both *C. difficile* toxin and *C. perfringens* iota toxin, suggesting that these features are common in other binary toxins including *C. spiroforme* toxin and *C. botulinum* C2 toxin. The binding and unfolding mechanism of the A-components of CDT and iota toxin have been considered to be similar to that of the anthrax toxin, but it was shown that CDT and iota toxin have a unique mechanism.

Whether the conformation of the φ-clamp is flexible or the secondary structure of the substrate unfolds during the translocation remains unclear. The φ-clamp structures seem stable in the same configuration as closed (6-Å diameter) in all reported structures of CDTb, Ib, and PA, and no other open conformation was observed. However, two assumed open-states have been observed in electrophysiological studies[43,45]. To address this, the high-resolution structure of the translocation complex needs to be clarified. Recently, the first attempt to determine the structure of the translocation complex of PA was made[46].

Novel pharmacological inhibition studies against pore-forming toxin have started in CDT. A designed symmetrical cyclodextrin molecule was shown to inhibit the CDTb-pore, as well as PA-pore, Ib-pore, and C2-pore[47–49]. Furthermore, chloroquinone and its derivatives were reported to inhibit intoxication as toxin pore blockers[50]. The present high resolution CDTa-bound CDTb-pore structures provide more insights for developing inhibitors to combat hypervirulent *C. difficile* infection.

Methods

CDTa and CDTb expression and purification

cdtA (Uniprot ID: Q9KH42, amino acids 51–463) was cloned into pET-23a with a C-terminal TEV-protease recognition site followed by a His-tag and overexpressed in *Escherichia coli* C41. The transformants were cultured in 150 mL of LB medium containing ampicillin (50 mg/mL) and 2% (w/v) glucose at 37 °C for 16 h. Glucose was added to suppress the expression of CDTa at an early stage of the culture. The preculture medium was inoculated into 1.35 L of LB medium containing ampicillin (final concentration: 50 mg/mL) but no glucose so that the growing cells could express CDTa. The total volume (1.5 L) of LB medium was cooled in an ice-water bucket. Isopropyl β-D-1-thiogalactopyranoside (IPTG) was added (final concentration: 0.5 mM), followed by culturing at 23 °C for 5 h. The harvested cells were suspended in lysis buffer containing 20 mM Tris (pH 8.0) and 20 mM imidazole, disrupted by sonication in ice–water, and centrifuged at 180,000 × *g* for 40 min. The supernatant was loaded onto a Ni-NTA agarose column. The column was washed with lysis buffer, and bound proteins, including CDTa, were eluted with a buffer containing 20 mM Tris (pH 8.0) and 500 mM imidazole. The eluted fractions were collected in an Amicon 30 K centrifugal tube to exchange the buffer with CDTa buffer containing 50 mM Tris (pH 8.0), 300 mM

NaCl, and 2.5 mM $CaCl_2$. The C-terminal His-tag was removed by incubating the fractions with TEV-protease (1/10 weight of CDTa) at 37 °C for 1 h. Proteolysis was terminated by adding phenylmethylsulphonyl fluoride (PMSF) (final concentration: 1 mM). The CDTa obtained was loaded onto SEC column Superdex 75 10/300 GL (Thermo Fisher Scientific) and eluted with a buffer containing 10 mM Tris (pH 8.0) and 100 mM NaCl at a flow rate of 0.5 mL/min. The fractions containing CDTa were collected and concentrated to 7.35 mg/mL using Amicon 30 K.

cdtB (Uniprot ID: o32739, amino acids 40–876) was cloned into pGEX4T-1 without the signal peptide and expressed in *E. coli* BL21 Star (DE3). The transformant was cultured in 1 L of super broth medium containing amipicillin (50 mg/mL) at 37 °C to an OD_{600} of 0.7. The culture medium was cooled on an ice–water bucket. IPTG (final concentration: 1 mM) was added to the culture medium, and the culture was incubated at 20 °C for 16 h. The harvested cells were suspended in lysis buffer containing 20 mM Tris (pH 8.0), 150 mM NaCl, 2 mM $CaCl_2$, and 5 mM dithiothreitol, and disrupted by sonication in ice–water. After centrifugation at 180,000 × *g* for 40 min, the supernatant was loaded onto a Glutathione Sepharose 4B resin (GE Healthcare) column. Then, the column was washed with lysis buffer and bound proteins, including CDTb, were eluted using a buffer containing 20 mM Tris (pH 8.0), 150 mM NaCl, and 10 mM reduced glutathione. The collected fractions were loaded onto the Amicon 50 K centrifugal tube to exchange the buffer with a buffer containing 20 mM Tris (pH 8.0), 50 mM NaCl, and 2.5 mM $CaCl_2$, followed by concentration to 1.1 mg/mL.

Sample preparation for cryo-EM

To remove the N-terminal 20-kDa pre-sequence and activate oligomerization, 1.1 mg of purified CDTb with the N-terminal GST-tag was treated with 1.1 mg of a-chymotrypsin for 1 h at 25 °C . Proteolysis was terminated by adding PMSF (final concentration: 1 mM). Then, the CDTb was incubated with LMNG (final concentration: 0.03% (w/v)) for 1 h at 37 °C, loaded onto a density gradient bed containing 10%–30% (v/v) glycerol, 50 mM HEPES (pH 7.5), 100 mM NaCl, 1 mM $CaCl_2$, and 0.003% (w/v) LMNG, and ultracentrifuged at 230,139 × *g* for 16 h. Subsequently, the centrifuge tube was punctured at the bottom with an injection needle and five drops were collected as a fraction. The presence of CDTb-pores was monitored by measuring A280 and performing sodium dodecyl sulphate–polyacrylamide gel electrophoresis. Fractions containing CDTb-pores were collected. Buffer was exchanged with a buffer containing 10 mM HEPES (pH 7.5), 1 mM $CaCl_2$, and 0.003% (w/v) LMNG using PD10 and concentrated to 1.58 mg/mL. For complex formation, CDTa without His-tag was added to the resultant CDTb-pore at a 3-fold molar excess.

Cryo-EM data collection and image processing

The purified CDTa-bound CDTb-pore was applied to a glow-discharged Quantifoil holey carbon grid (R1.2/1.3, Cu, 300 mech), blotted for 4.5 s at 4 °C in 100% humidity and plunged into frozen liquid ethane using a Vitrobot Mark IV (Thermo Fisher Scientific). The grid was inserted into a Titan Krios (Thermo Fisher Scientific) operating at an acceleration voltage of 300 kV and equipped with a Cs corrector (CEOS, GmbH). Cryo-EM images were recorded with a K3 direct electron detector (Gatan) in counting mode with an energy filter at a slit width of 20 eV. Data were automatically collected using the SerialEM software (https://bio3d.colorado.edu/SerialEM/) at a physical pixel size of 0.88 Å/pixel with a defocus range from −0.8 to −2.0 μm at 50 e/Å^2 with 3.36 s exposure.

The movie frames were subsequently aligned to correct for beam-induced movement and drift using MotionCor2[51], and contrast transfer function (CTF) was evaluated using Gctf[52]. Approximately 1,000 particles were manually selected from 10 micrographs to perform two-dimensional (2D) classification. Using a good 2D class average image, a total of 2,608,418 particle images were automatically picked, and several rounds of 2D classifications were performed using RELION-3.1[53]. A total of 735,102 particles were selected for building the initial model of the CDTa-bound CDTb-pore using cryoSPARC2[54] and subjected to 3D classification into 10 classes using RELION-3.1, as shown in Supplementary Fig. S2. For the CDTa-bound CDTb-pore, a good 3D class was selected and subjected to 3D classification into three classes. In class 1, the D4 domain of CDTb was clearly visible. By contrast, the D4 domain was not visible in class 2. The particles of classes 1 and 2 were re-extracted with a pixel size of 0.88 Å/pixel and subjected to three 3D refinements, two CTF refinements, and Bayesian polishing. Afterwards, 3D refinement and CTF refinement were repeated. For class 2 subsets, no-align 3D classification using a mask focusing on the CDTa region improved the local resolution of CDTa. Final 3D refinement and post-processing yielded maps with global resolutions of 2.64-Å (class 1) and 2.56-Å (class 2), according to the 0.143 criterion of the FSC. Local resolution was estimated using RELION-3.1. The processing strategy is described in Supplementary Fig. S2.

Analysis of the di-heptamer of the CDTa-bound CDTb-pore was performed as follows: from the best class of the 3D classification containing 146,821 particles, duplicated particles were removed, and the remaining particles were re-extracted to a pixel size of 0.88 Å/pixel. A total of 102,116 particles were subjected to 3D refinement and CTF refinement. The final 3D refinement and post-processing yielded maps with global resolutions of 3.19-Å, according to the 0.143 criterion of the FSC. One of the heptamers was subtracted from the di-heptamer of the CDTa-bound CDTb-pore and subjected to three 3D refinements and two CTF refinements. The final 3D refinement and post-processing yielded maps with global resolutions of 2.95-Å, according to the 0.143 criterion of the FSC. The processing strategy is described in Supplementary Fig. S2.

Model building and refinement

CDTa-bound CDTb-pore (class 1). The model of the CDTa-bound CDTb-pore was built using the cryo-EM density map of class 1 pore. The initial rigid-body fit of the CDTa structure (PDB ID: 6V1S) and CDTb-pore structure (PDB ID: 6UWR) were applied to the map using UCSF Chimera. They were manually modified and refined using iterative rounds of COOT[55] and PHENIX[56]. The model of the tip of the b-barrel (337–358) was not built because of weak map density. Using the model which was refined against map of class 2, The residues (480-500) containing NSS-loops at in and out conformations were replaced into the model of class 1. The combined model was further modified and refined using iterative rounds of COOT and PHENIX.

CDTa-bound CDTb-pore (class 2). The model of the CDTa-bound CDTb-pore (class 1) was fitted into the cryo-EM density map of class 2 using UCSF Chimera[57]. The tip of the b-barrel (332–336 and 359–363) and D4-II (743–876) were excluded because of poor map density. The final model was manually modified and refined using iterative rounds of COOT and PHENIX. During model refinement, the map of NSS-loops revealed two conformations in some protomer. Thus, in subunits A, B, D, E and G, both “in” and “out” conformations of NSS-loop were constructed and refined against the map of class 2, with the occupancy of each conformation at 0.5:0.5. They were further manually modified and refined using iterative rounds of COOT and PHENIX.

For both structures, the flip states of the side-chain Asn, Gln, and His residues were validated and corrected by protonation using MolProbity[58]. Gold-standard FSC curves of the final map, and FSC curves for cross-validation between the map and model, were evaluated using RELION-3.1 and comprehensive validation in PHENIX, respectively. All figures were prepared using PyMOL (https://pymol.org/2/), UCSF Chimera, and UCSF ChimeraX[59].

Declarations

Data availability statement

The Cryo-EM maps and coordinates were deposited to the Electron Microscopy Data Bank (EMDB) and Protein Data Bank (PDB) with the accession codes EMDB-32043 and PDB 7VNN for CDTa-bound CDTb-pore class 1, and EMDB-32041 and PDB 7VNJ for CDTa-bound CDTb-pore class 2, respectively.

Acknowledgements

This work was supported by JSPS KAKENHI Grant Numbers 18K06170 and 21H02452 (to H.T) and JST PRESTO Grant Number JPMJPR21E5 (to A.K). This research was partially supported by Platform Project for Supporting Drug Discovery and Life Science Research (Basis for Supporting Innovative Drug Discovery and Life Science Research (BINDS)) from AMED under Grant Number 2366.

Author contributions

All author participated in research design; T.Yamada prepared the CDTb-pore and CDTa-bound CDTb-pore for cryo-EM; A.K. and T.K. performed cryo-EM data acquisition and A.K. and T.Yamada performed image processing and data analysis; T.Yamada and T.Yoshida performed the atomic model building, structure refinement and analyses; all author contributed to writing the manuscript and H.T. supervise the project. We thank S. Suzuki, S. Tomoda, and S. Onda of the members of Structural Biology Laboratory in Kyoto Sangyo University for help of the manuscript preparation.

Author information

Competing interests: The authors declare no competing interests.

Correspondence and requests for materials should be addressed to corresponding H.T. (tsuge@cc.kyoto-su.ac.jp)

References

1 Wickner, W. & Schekman, R. Protein translocation across biological membranes. *Science* **310**, 1452-1456, doi:10.1126/science.1113752 (2005).

2 Jomaa, A., Boehringer, D., Leibundgut, M. & Ban, N. Structures of the E. coli translating ribosome with SRP and its receptor and with the translocon. *Nat Commun* **7**, 10471, doi:10.1038/ncomms10471 (2016).

3 Jomaa, A. *et al.* Structure of the quaternary complex between SRP, SR, and translocon bound to the translating ribosome. *Nat Commun* **8**, 15470, doi:10.1038/ncomms15470 (2017).

4 Costa, T. R. *et al.* Secretion systems in Gram-negative bacteria: structural and mechanistic insights. *Nat Rev Microbiol* **13**, 343-359, doi:10.1038/nrmicro3456 (2015).

5 Miletic, S. *et al.* Substrate-engaged type III secretion system structures reveal gating mechanism for unfolded protein translocation. *Nat Commun* **12**, 1546, doi:10.1038/s41467-021-21143-1 (2021).

6 Gao, X. *et al.* Structural Insight Into Conformational Changes Induced by ATP Binding in a Type III Secretion-Associated ATPase From Shigella flexneri. *Front Microbiol* **9**, 1468, doi:10.3389/fmicb.2018.01468 (2018).

7 Gibert, M., Petit, L., Raffestin, S., Okabe, A. & Popoff, M. R. Clostridium perfringens iota-toxin requires activation of both binding and enzymatic components for cytopathic activity. *Infect Immun* **68**, 3848-3853, doi:10.1128/IAI.68.7.3848-3853.2000 (2000).

8 Stiles, B. G., Hale, M. L., Marvaud, J. C. & Popoff, M. R. Clostridium perfringens iota toxin: characterization of the cell-associated iota b complex. *Biochem J* **367**, 801-808, doi:10.1042/BJ20020566 (2002).

9 Nagahama, M. *et al.* Binding and internalization of Clostridium perfringens iota-toxin in lipid rafts. *Infect Immun* **72**, 3267-3275 (2004).

10 Gibert, M. *et al.* Differential requirement for the translocation of clostridial binary toxins: iota toxin requires a membrane potential gradient. *FEBS Lett* **581**, 1287-1296, doi:10.1016/j.febslet.2007.02.041 (2007).

11 Knapp, O., Benz, R. & Popoff, M. R. Pore-forming activity of clostridial binary toxins. *Biochim Biophys Acta* **1858**, 512-525, doi:10.1016/j.bbamem.2015.08.006 (2016).

12 Papatheodorou, P. *et al.* Lipolysis-stimulated lipoprotein receptor (LSR) is the host receptor for the binary toxin Clostridium difficile transferase (CDT). *Proc Natl Acad Sci U S A* **108**, 16422-16427, doi:10.1073/pnas.1109772108 (2011).

13 Papatheodorou, P. *et al.* Identification of the cellular receptor of Clostridium spiroforme toxin. *Infect Immun* **80**, 1418-1423, doi:10.1128/IAI.06378-11 (2012).

14 Papatheodorou, P., Barth, H., Minton, N. & Aktories, K. Cellular Uptake and Mode-of-Action of Clostridium difficile Toxins. *Adv Exp Med Biol* **1050**, 77-96, doi:10.1007/978-3-319-72799-8_6 (2018).

15 Haug, G., Aktories, K. & Barth, H. The host cell chaperone Hsp90 is necessary for cytotoxic action of the binary iota-like toxins. *Infect Immun* **72**, 3066-3068, doi:10.1128/IAI.72.5.3066-3068.2004 (2004).

16 Ernst, K. *et al.* Hsp70 facilitates trans-membrane transport of bacterial ADP-ribosylating toxins into the cytosol of mammalian cells. *Sci Rep* **7**, 2724, doi:10.1038/s41598-017-02882-y (2017).

17 Aktories, K. *et al.* Botulinum C2 toxin ADP-ribosylates actin. *Nature* **322**, 390-392 (1986).

18 Vandekerckhove, J., Schering, B., Barmann, M. & Aktories, K. Clostridium perfringens iota toxin ADP-ribosylates skeletal muscle actin in Arg-177. *FEBS Lett* **225**, 48-52 (1987).

19 Han, S., Craig, J. A., Putnam, C. D., Carozzi, N. B. & Tainer, J. A. Evolution and mechanism from structures of an ADP-ribosylating toxin and NAD complex. *Nat Struct Biol* **6**, 932-936 (1999).

20 Tsuge, H. *et al.* Crystal structure and site-directed mutagenesis of enzymatic components from Clostridium perfringens iota-toxin. *J Mol Biol* **325**, 471-483 (2003).

21 Tsuge, H. *et al.* Structural basis of actin recognition and arginine ADP-ribosylation by Clostridium perfringens iota-toxin. *Proc Natl Acad Sci U S A* **105**, 7399-7404, doi:0801215105 [pii]10.1073/pnas.0801215105 (2008).

22 Sundriyal, A., Roberts, A. K., Shone, C. C. & Acharya, K. R. Structural basis for substrate recognition in the enzymatic component of ADP-ribosyltransferase toxin CDTa from Clostridium difficile. *J Biol Chem* **284**, 28713-28719, doi:10.1074/jbc.M109.043018 (2009).

23 Jiang, J., Pentelute, B. L., Collier, R. J. & Zhou, Z. H. Atomic structure of anthrax protective antigen pore elucidates toxin translocation. *Nature* **521**, 545-549, doi:10.1038/nature14247 (2015).

24 Gerding, D. N., Johnson, S., Rupnik, M. & Aktories, K. Clostridium difficile binary toxin CDT: mechanism, epidemiology, and potential clinical importance. *Gut Microbes* **5**, 15-27, doi:10.4161/gmic.26854 (2014).

25 Stubbs, S. *et al.* Production of actin-specific ADP-ribosyltransferase (binary toxin) by strains of Clostridium difficile. *FEMS Microbiol Lett* **186**, 307-312 (2000).

26 Chandrasekaran, R. & Lacy, D. B. The role of toxins in Clostridium difficile infection. *FEMS Microbiol Rev* **41**, 723-750, doi:10.1093/femsre/fux048 (2017).

27 McDonald, L. C. *et al.* An epidemic, toxin gene-variant strain of Clostridium difficile. *N Engl J Med* **353**, 2433-2441, doi:10.1056/NEJMoa051590 (2005).

28 Loo, V. G. *et al.* A predominantly clonal multi-institutional outbreak of Clostridium difficile-associated diarrhea with high morbidity and mortality. *N Engl J Med* **353**, 2442-2449, doi:10.1056/NEJMoa051639 (2005).

29 Goorhuis, A. *et al.* Emergence of Clostridium difficile infection due to a new hypervirulent strain, polymerase chain reaction ribotype 078. *Clin Infect Dis* **47**, 1162-1170, doi:10.1086/592257 (2008).

30 Rupnik, M. Heterogeneity of large clostridial toxins: importance of Clostridium difficile toxinotypes. *FEMS Microbiol Rev* **32**, 541-555, doi:10.1111/j.1574-6976.2008.00110.x (2008).

31 Debast, S. B. *et al.* Clostridium difficile PCR ribotype 078 toxinotype V found in diarrhoeal pigs identical to isolates from affected humans. *Environ Microbiol* **11**, 505-511, doi:10.1111/j.1462-2920.2008.01790.x (2009).

32 Schwan, C. *et al.* Clostridium difficile toxin CDT hijacks microtubule organization and reroutes vesicle traffic to increase pathogen adherence. *Proc Natl Acad Sci U S A* **111**, 2313-2318, doi:10.1073/pnas.1311589111 (2014).

33 Cowardin, C. A. *et al.* The binary toxin CDT enhances Clostridium difficile virulence by suppressing protective colonic eosinophilia. *Nat Microbiol* **1**, 16108, doi:10.1038/nmicrobiol.2016.108 (2016).

34 Anderson, D. M., Sheedlo, M. J., Jensen, J. L. & Lacy, D. B. Structural insights into the transition of Clostridioides difficile binary toxin from prepore to pore. *Nat Microbiol* **5**, 102-107, doi:10.1038/s41564-019-0601-8 (2020).

35 Xu, X. *et al.* Structure of the cell-binding component of the Clostridium difficile binary toxin reveals a di-heptamer macromolecular assembly. *Proc Natl Acad Sci U S A* **117**, 1049-1058, doi:10.1073/pnas.1919490117 (2020).

36 Sheedlo, M. J., Anderson, D. M., Thomas, A. K. & Lacy, D. B. Structural elucidation of the Clostridioides difficile transferase toxin reveals a single-site binding mode for the enzyme. *Proc Natl Acad Sci U S A* **117**, 6139-6144, doi:10.1073/pnas.1920555117 (2020).

37 Yamada, T. & Tsuge, H. Preparation of Clostridium perfringens binary iota-toxin pore complex for structural analysis using cryo-EM. *Methods Enzymol* **649**, 125-148, doi:10.1016/bs.mie.2021.01.032 (2021).

38 Rosenthal, P. B. & Henderson, R. Optimal determination of particle orientation, absolute hand, and contrast loss in single-particle electron cryomicroscopy. *J Mol Biol* **333**, 721-745, doi:10.1016/j.jmb.2003.07.013 (2003).

39 Scheres, S. H. RELION: implementation of a Bayesian approach to cryo-EM structure determination. *J Struct Biol* **180**, 519-530, doi:10.1016/j.jsb.2012.09.006 (2012).

40 Krantz, B. A. *et al.* A phenylalanine clamp catalyzes protein translocation through the anthrax toxin pore. *Science* **309**, 777-781, doi:10.1126/science.1113380 (2005).

41 Yamada, T. *et al.* Cryo-EM structures reveal translocational unfolding in the clostridial binary iota toxin complex. *Nat Struct Mol Biol* **27**, 288-296, doi:10.1038/s41594-020-0388-6 (2020).

42 Hardenbrook, N. J. *et al.* Atomic structures of anthrax toxin protective antigen channels bound to partially unfolded lethal and edema factors. *Nat Commun* **11**, 840, doi:10.1038/s41467-020-14658-6 (2020).

43 Das, D. & Krantz, B. A. Peptide- and proton-driven allosteric clamps catalyze anthrax toxin translocation across membranes. *Proc Natl Acad Sci U S A* **113**, 9611-9616, doi:10.1073/pnas.1600624113 (2016).

44 Simon, S. M., Peskin, C. S. & Oster, G. F. What drives the translocation of proteins? *Proc Natl Acad Sci U S A* **89**, 3770-3774, doi:10.1073/pnas.89.9.3770 (1992).

45 Yamini, G. *et al.* Hydrophobic Gating and 1/f Noise of the Anthrax Toxin Channel. *J Phys Chem B* **125**, 5466-5478, doi:10.1021/acs.jpcb.0c10490 (2021).

46 Machen, A. J., Fisher, M. T. & Freudenthal, B. D. Anthrax toxin translocation complex reveals insight into the lethal factor unfolding and refolding mechanism. *Sci Rep* **11**, 13038, doi:10.1038/s41598-021-91596-3 (2021).

47 Nestorovich, E. M., Karginov, V. A., Berezhkovskii, A. M. & Bezrukov, S. M. Blockage of anthrax PA63 pore by a multicharged high-affinity toxin inhibitor. *Biophys J* **99**, 134-143, doi:10.1016/j.bpj.2010.03.070 (2010).

48 Bezrukov, S. M. *et al.* Interactions of high-affinity cationic blockers with the translocation pores of B. anthracis, C. botulinum, and C. perfringens binary toxins. *Biophys J* **103**, 1208-1217, doi:10.1016/j.bpj.2012.07.050 (2012).

49 Roeder, M. *et al.* Tailored cyclodextrin pore blocker protects mammalian cells from clostridium difficile binary toxin CDT. *Toxins (Basel)* **6**, 2097-2114, doi:10.3390/toxins6072097 (2014).

50 Ernst, K. *et al.* Characterization and Pharmacological Inhibition of the Pore-Forming Clostridioides difficile CDTb Toxin. *Toxins (Basel)* **13**, doi:10.3390/toxins13060390 (2021).

51 Zheng, S. Q. *et al.* MotionCor2: anisotropic correction of beam-induced motion for improved cryo-electron microscopy. *Nat Methods* **14**, 331-332, doi:10.1038/nmeth.4193 (2017).

52 Zhang, K. Gctf: Real-time CTF determination and correction. *J Struct Biol* **193**, 1-12, doi:10.1016/j.jsb.2015.11.003 (2016).

53 Zivanov, J. *et al.* New tools for automated high-resolution cryo-EM structure determination in RELION-3. *Elife* **7**, doi:10.7554/eLife.42166 (2018).

54 Punjani, A., Rubinstein, J. L., Fleet, D. J. & Brubaker, M. A. cryoSPARC: algorithms for rapid unsupervised cryo-EM structure determination. *Nat Methods* **14**, 290-296, doi:10.1038/nmeth.4169 (2017).

55 Emsley, P. & Cowtan, K. Coot: model-building tools for molecular graphics. *Acta Crystallogr D Biol Crystallogr* **60**, 2126-2132, doi:S0907444904019158 [pii]

10.1107/S0907444904019158 (2004).

56 Afonine, P. V. *et al.* Real-space refinement in PHENIX for cryo-EM and crystallography. *Acta Crystallogr D Struct Biol* **74**, 531-544, doi:10.1107/S2059798318006551 (2018).

57 Pettersen, E. F. *et al.* UCSF Chimera--a visualization system for exploratory research and analysis. *J Comput Chem* **25**, 1605-1612, doi:10.1002/jcc.20084 (2004).

58 Chen, V. B. *et al.* MolProbity: all-atom structure validation for macromolecular crystallography. *Acta Crystallogr D Biol Crystallogr* **66**, 12-21, doi:10.1107/S0907444909042073 (2010).

59 Goddard, T. D. *et al.* UCSF ChimeraX: Meeting modern challenges in visualization and analysis. *Protein Sci* **27**, 14-25, doi:10.1002/pro.3235 (2018).

60 Smart, O. S., Neduvelil, J. G., Wang, X., Wallace, B. A. & Sansom, M. S. HOLE: a program for the analysis of the pore dimensions of ion channel structural models. *J Mol Graph* **14**, 354-360, 376, doi:10.1016/s0263-7855(97)00009-x (1996).

61 Robert, X. & Gouet, P. Deciphering key features in protein structures with the new ENDscript server. *Nucleic Acids Res* **42**, W320-324, doi:10.1093/nar/gku316 (2014).

Tables

	Class 1	Class 2
Data collection and processing		
Magnification	81,000	81,000
Voltage (kV)	300	300
Electron exposure ($e^-/Å^2$)	50	50
Defocus range (mm)	-0.8 to -2.0	-0.8 to -2.0
Pixel size (Å)	0.88	0.88
Symmetry imposed	C1	C1
Initial particle images (no.)	2,608,418	2,608,418
Final particle images (no.)	83,061	173,260
Map resolution (Å)	2.64	2.56
FSC threshold	0.143	0.143
Map resolution range (Å)	2.41-6.5	2.34-6.2
Map sharpening *B* factor ($Å^2$)	-32.2638	-36.3530
Refinement		
Initial model used	6UWR, 6V1S	6UWR, 6V1S
Model resolution (Å)	3.2	2.7
FSC threshold	0.5	0.5
Model composition		
Non-hydrogen atoms	38,842	30,682
Protein residues	4,863	3,856
Ligands	21	21
***B* factors ($Å^2$)**		
Protein	91.30	93.69
Ligand	74.31	77.75
R.m.s deviations		
Bond lengths (Å)	0.004	0.004
Bond angles (°)	0.941	0.948
Validation		
MolProbity score	1.75	1.67
Clashscore	6.11	6.10
Poor rotamers (%)	0.00	0.20
Ramachandran plot		
Favored (%)	93.85	95.16
Allowed (%)	6.15	4.84
Disallowed (%)	0.00	0.00

Table 1

Cryo-EM data collection, refinement and validation statistics

Figures

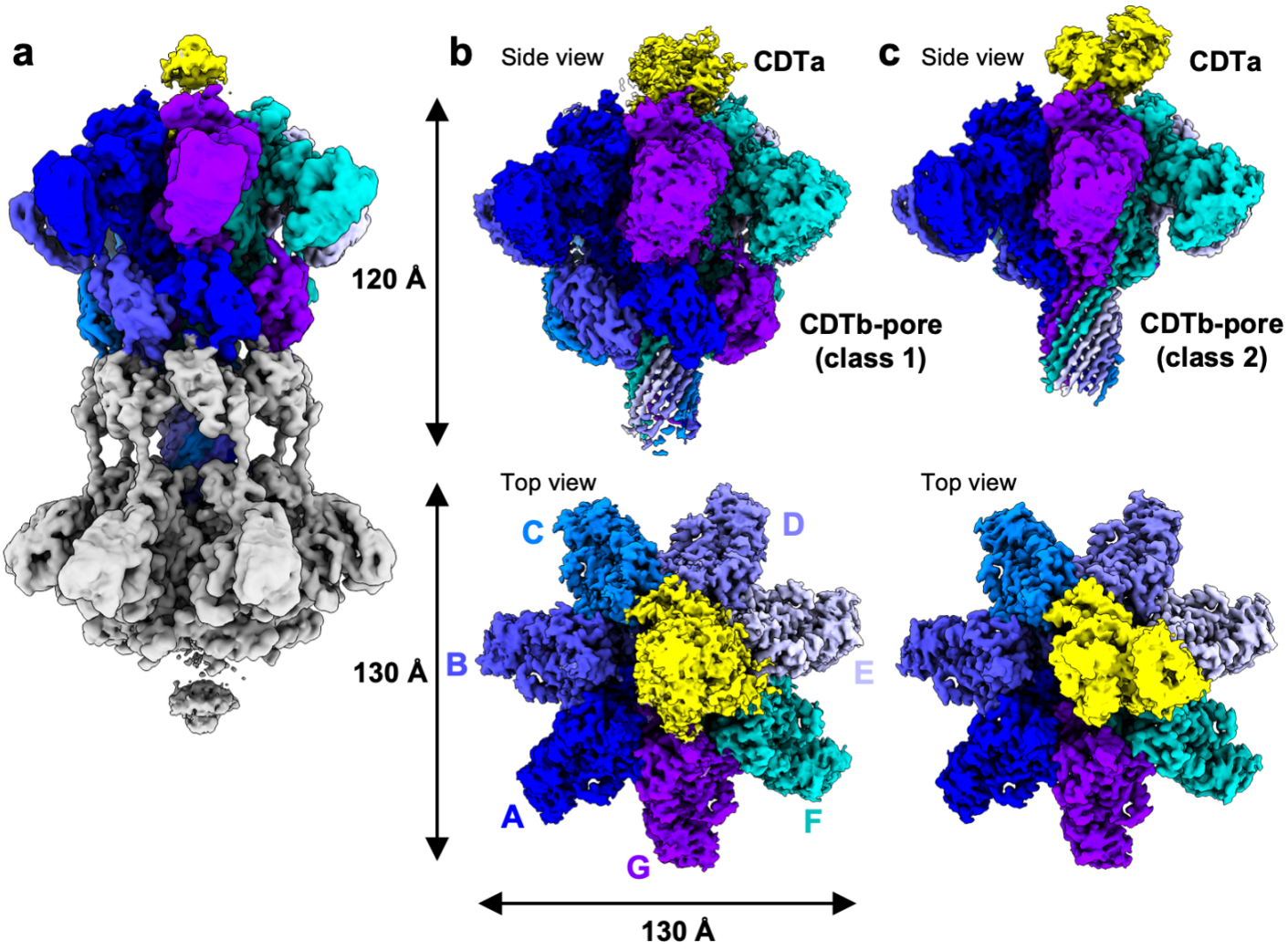

Figure 1

Cryo-EM density maps of the CDTa-bound CDTb-pores a CDTa-bound di-heptamer CDTb. b CDTa-bound CDTb-pore (class 1) of top view and side view. c CDTa-bound CDTb pore (class 2) of top view and side view. Each protomer of the CDTb-pore and CDTa is coloured.

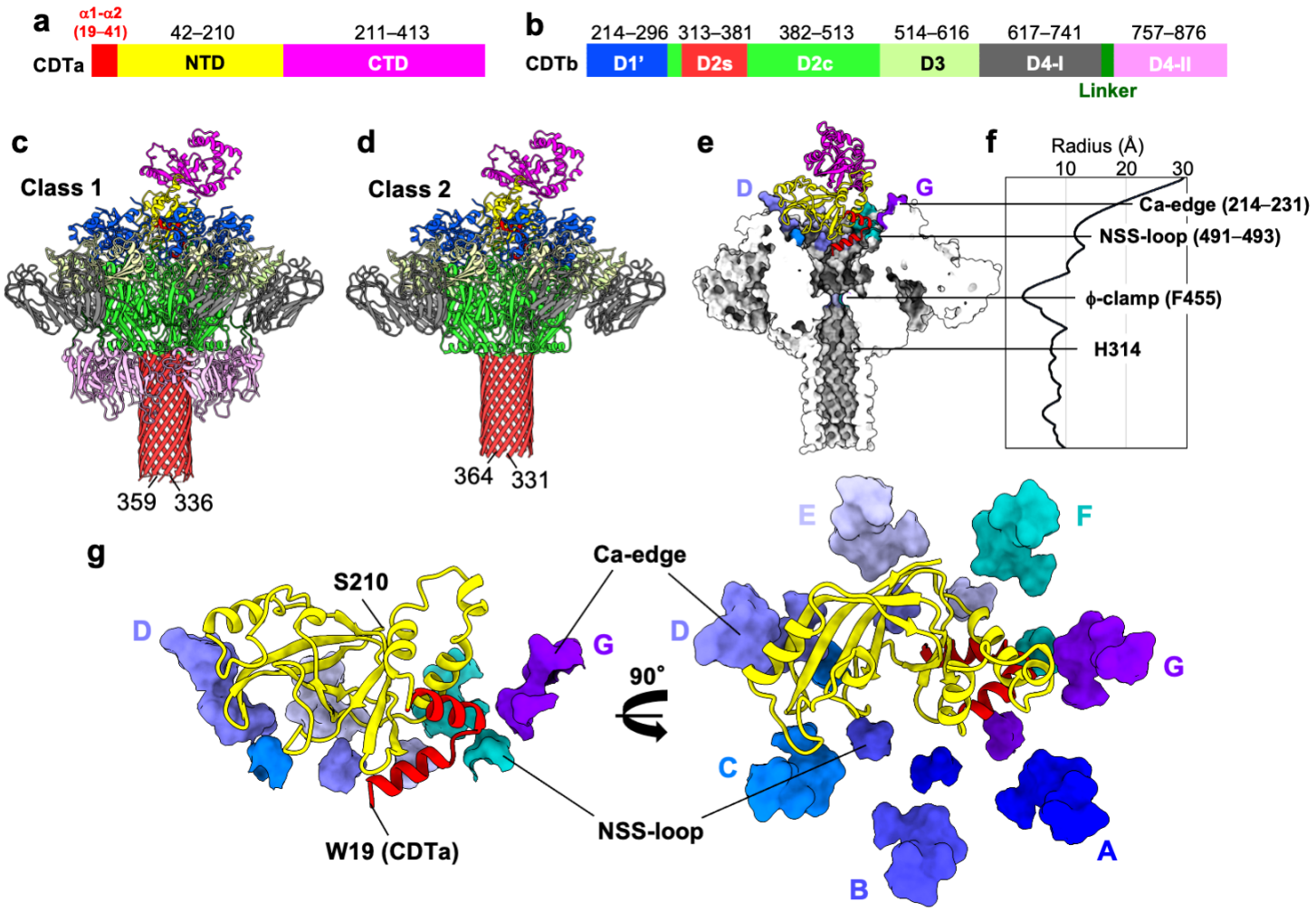

Figure 2

Atomic structures of the CDTa-bound CDTb-pores a Schematic domain structure of CDTa. b Schematic domain structure of CDTb after cleavage of the N-terminal pro-sequence. c Structure of the CDTa-bound CDTb-pore (class 1). d Structure of the CDTa-bound CDTb-pore (class 2). Color are shown as the same as the schematic domains a and b. e Cut-away view of the CDTa-bound CDTb-pore. The CDTb-pore are shown as surface model, in which Ca-edges are coloured by the respective protomer. CDTa structure is shown as ribbon model. f Diagrammatic representation of the diameter of the CDTb-pore. The diameter was measured in the CDTb-pore structure as the CDTa-bound state (class 2) using the HOLE software60. g Interaction between CDTa and CDTb. The CDTa structure is shown as a ribbon model. Constriction sites (Ca-edges and NSS-loops) of the CDTb-pore are shown as surface model coloured by the respective protomer.

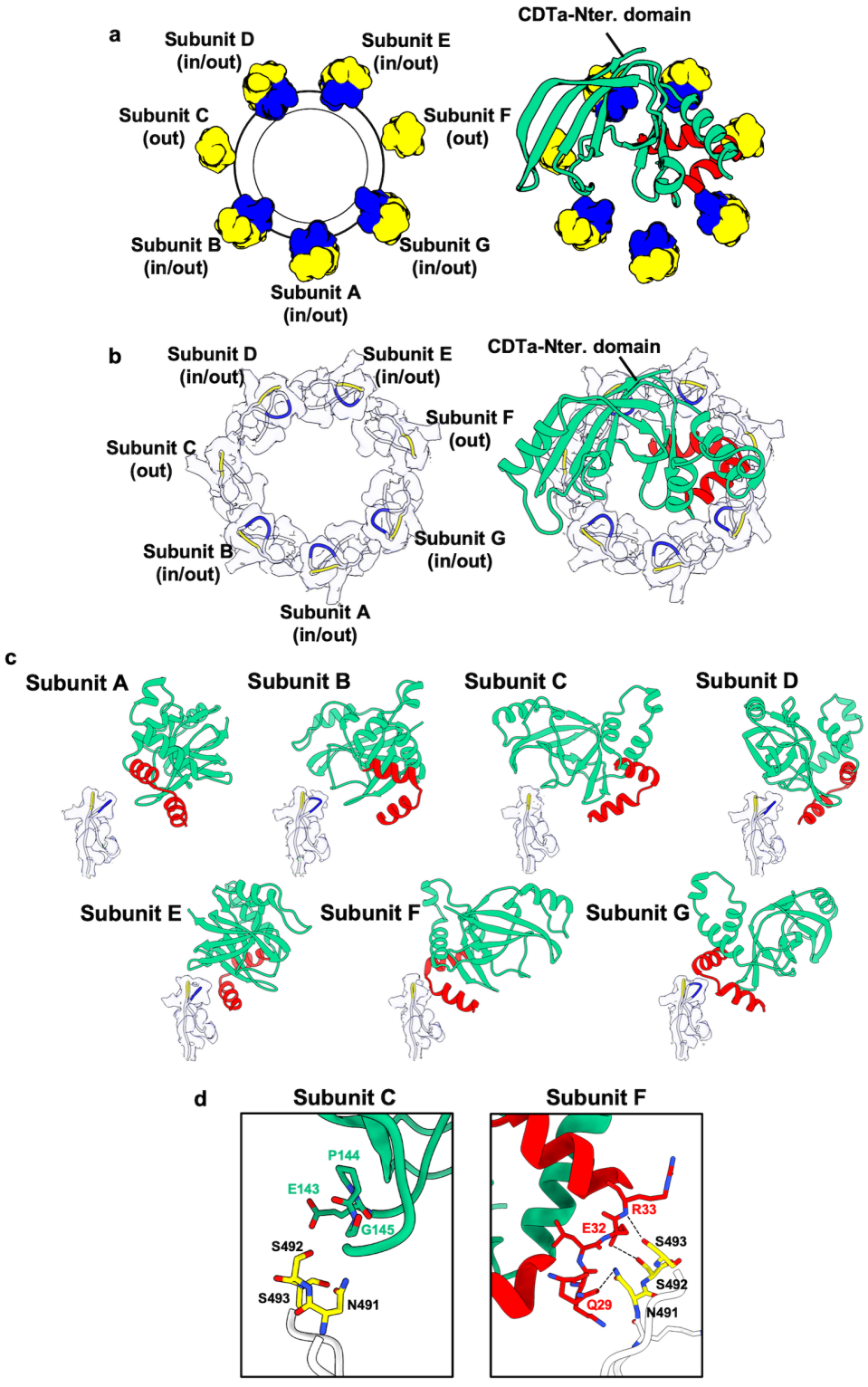

Figure 3

Conformations of the NSS-loop of the CDTb-pore a left, Conformations of the NSS-loops of the CDTb-pore in the CDTa-bound state are shown without CDTa. right, The same as fig. 3a, but with CDTa. The two circles are drawn as concentric circles of NSS-loops. The blue NSS-loops indicate in state and the yellow NSS-loops indicate out state. b left, Cryo-EM map of the NSS-loops of the CDTb-pore in the CDTa-bound state. right, Cryo-EM map of the NSS-loops of the CDTb-pore in the CDTa-bound state with CDTa. c The

close up views of “In” and “out” conformations of the NSS-loops of all chains A¬¬–G with the cryo-EM map. d Interactions between CDTa and NSS-loops of chains C and F. The two α-helices (α1–α2) and other N-terminal domain of CDTa is colorued as red and green, respectively. NSS-loops of CDTb are colorued as in (blue) and out (yellow), respectively.

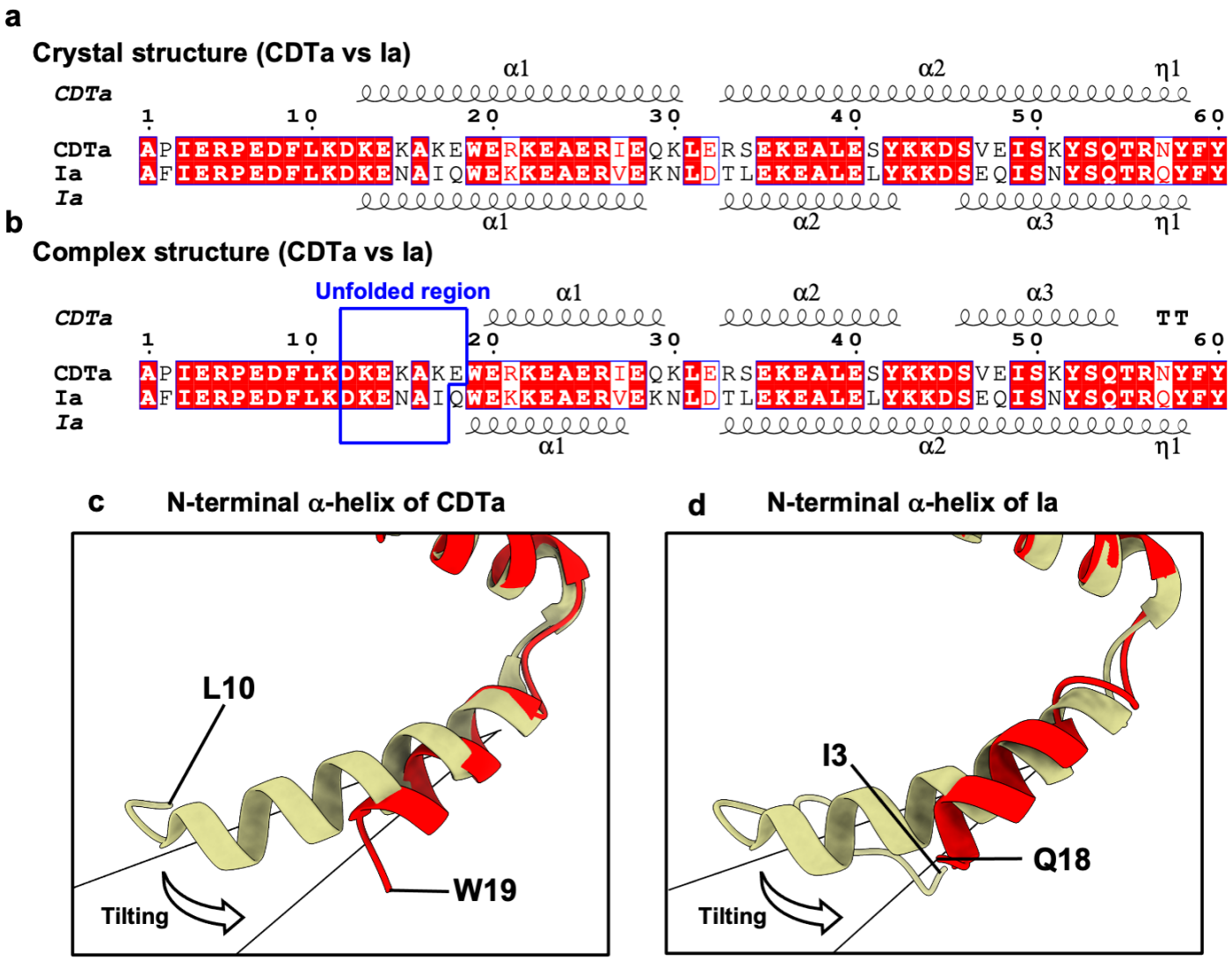

Figure 4

N-terminal α-helix conformational change of CDTa and Ia a The secondary structures of CDTa and Ia in their crystal structures. b The secondary structures of CDTa and Ia in their complexes. c Comparison of CDTa N-termininus between crystal structure of CDTa alone (PDB ID: 2WN6) and the present complex structure of CDTa and CDTb. d Comparison of Ia N-termininus between crystal structure of Ia alone (PDB ID: 1GIQ) and complex structure of Ia and Ib (PDB ID: 6KLO).

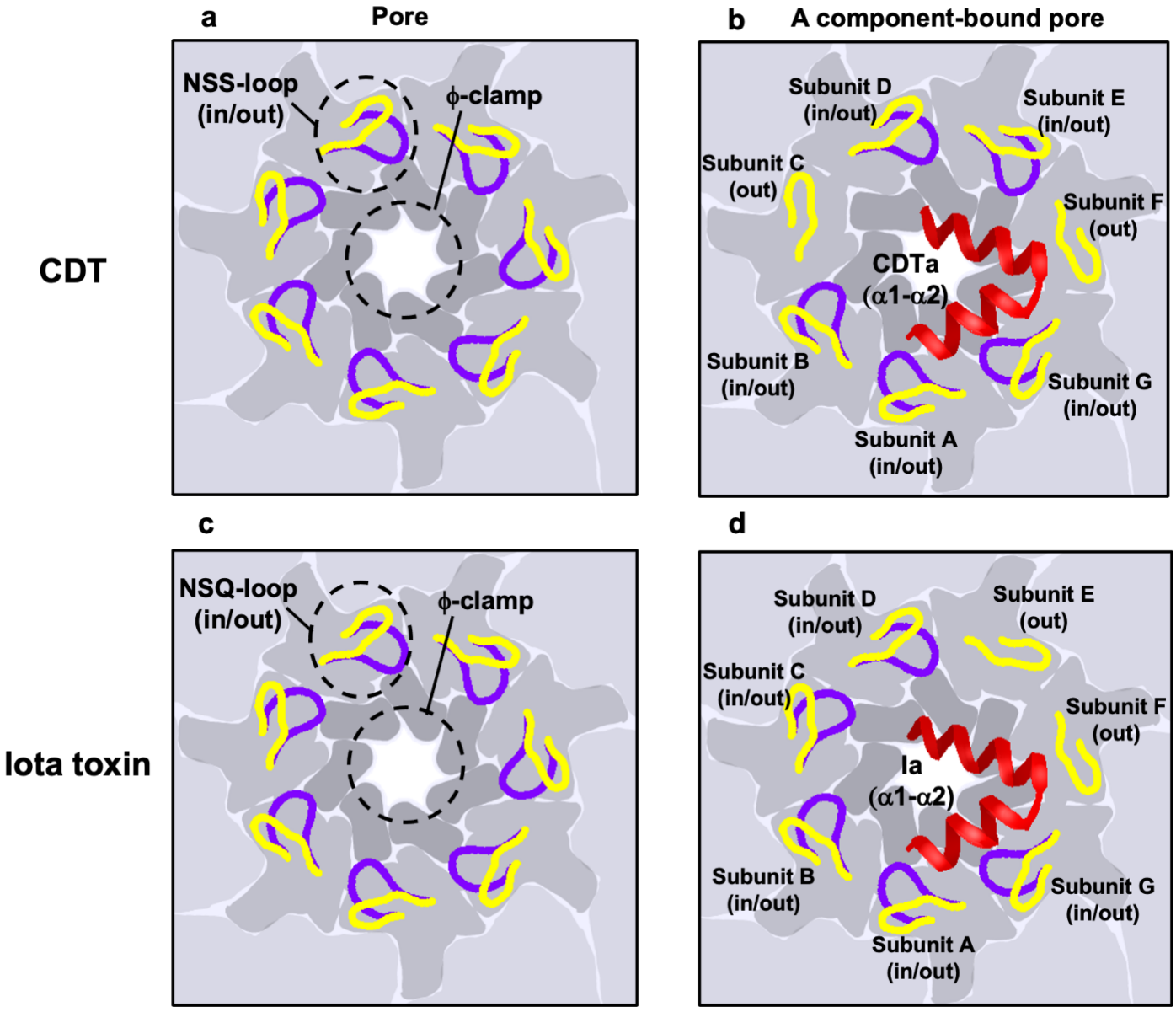

Figure 5

Depicted model showing NSS-loops and NSQ-loops with the N-terminal α-helix of CDTa and Ia a Both conformations “in” and “out” of NSS-loops are observed in the CDTb-pore. b In only subunit C and F, conformations were biased to “in” of NSS-loops caused by binding of CDTa. c Both conformations in and out of NSS-loops are observed in the Ib-pore. d In only subunit E and F, conformations were biased to “in” of NSQ-loops of the Ib-pore caused by binding of Ia. NSS-loops and NSQ-loops are shown as purple (in) and yellow (out).

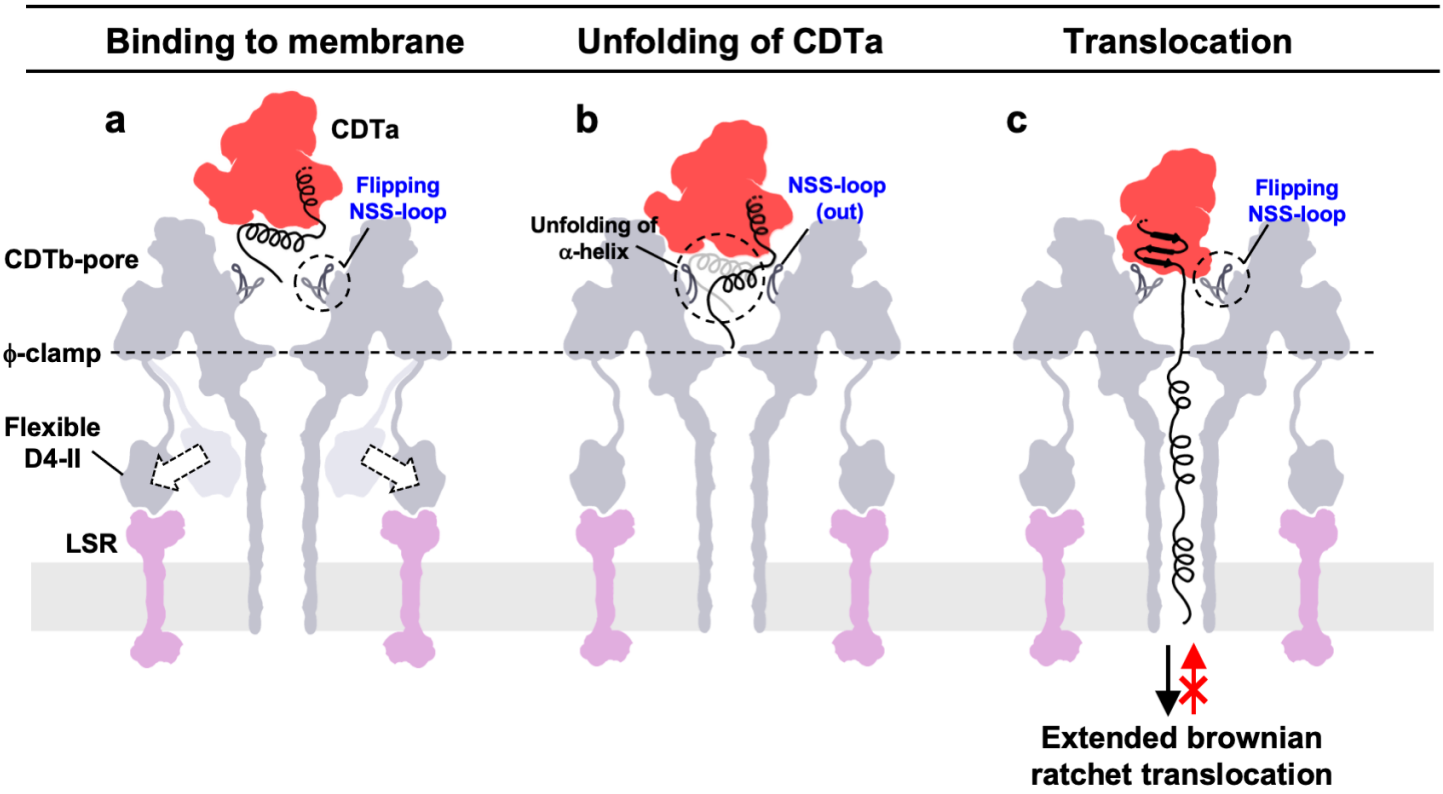

Figure 6

Translocation model of CDTa via CDTb-pore a CDTb-pore binding to LSR through the flexible D4-II domain. NSS-loops can be seen flipping. b Upon CDTa-binding on the NSS-loops of CDTb, the N-terminal α-helix of CDTa is partially unfolded and is tilted at 20°. c Unfolded CDTa is translocated via the Φ-clamp, with a 6Å diameter, using the ΔpH-driven Brownian ratchet model.

Supplementary Files

This is a list of supplementary files associated with this preprint. Click to download.

- ValidationReports.pdf
- ReportingsummaryTY.pdf
- Supplementarydata.pdf